



OPEN

# Strengthening the mechanical characteristics and cathodic delamination resistance of fiber-reinforced polymer through chemical surface modification of glass fibers

M. Shariatmadar<sup>1</sup>, S. Feizollahi<sup>1</sup>, P. Gholamhosseini<sup>1</sup>, Z. Abdorrezaee<sup>1</sup>, S. Ghorbanzadeh<sup>1</sup>, F. S. Hosseini<sup>1</sup>, F. Azad Shahraki<sup>2</sup> & M. Mahdavian<sup>1</sup>✉

This work aims to scrutinize the effect of the silanization of glass fibers (GF) on the mechanical properties and cathodic disbonding resistance of an epoxy composite coating. Successful silanization was approved based on different characterization techniques, including Fourier transform infrared spectra, field emission-scanning electron microscopy (FE-SEM), energy-dispersive X-ray spectroscopy, and thermogravimetric analysis. Tensile strength measurement exhibited a significant effect of silanization on the mechanical performance of the fiber-reinforced polymer (FRP). FE-SEM cross-sectional images illustrated improved interfacial bonding between the epoxy matrix and GF upon silanization. Pull-off measurements revealed improved wet adhesion strength of the FRP to the mild steel surface after exposure to the salt spray chamber when the GF were silanized. In addition, silanization revealed enhanced resistance to cathodic delamination (CD). Electrochemical impedance spectroscopy and electrochemical noise assessments proved silanization's significant influence on the FRP's CD resistance.

Epoxy polymers are broadly utilized as popular corrosion protection coatings in different applications due to their many exceptional properties, including excellent chemical resistance, toughness, shrinkage resistance, and adhesion<sup>1-4</sup>. Epoxy coatings act as an efficient barrier to water/corrosive species transfer to the metal substrates and increase their service life by reducing the corrosion rate from severe corrosive media. Polymer coatings can significantly decrease metallic structure corrosion via three dominant mechanisms: barrier, inhibition, and sacrificial<sup>5-9</sup>.

Generally, the organic coatings are relatively penetrable to water, oxygen, and corrosive species. Hence, after being exposed to corrosive electrolytes, the coatings undergo a degradation process, usually by forming defects such as cracking and delamination<sup>10,11</sup>. This also leads to a severe decrement in the barrier performance of the coating, leading to the penetration of more water and corrosive species into the interface of coating and substrate and acceleration of the metal corrosion rate. Loss of adhesion and delamination of the coating expands the cathodic and anodic areas increasing the rate of electrochemical reactions.

Various factors, such as interfacial interactions between the substrate and the polymeric coating, influence the robustness of the coating in corrosive media<sup>12</sup>. Many efforts have been made to enhance the coatings' adhesion to metallic substrates because the loss of adhesion directly affects the protective behaviors of polymeric coatings<sup>13,14</sup>.

Studies have shown that various additives or anticorrosion pigments increase the barrier functionality and protection features of polymeric coatings<sup>15</sup>. Recently, a variety of micro/nano reinforcers in the polymer matrix have been used to produce efficient composite coatings with higher mechanical strength, corrosion protection, and thermal and chemical stability<sup>16-19</sup>. The utilized nanoparticles in literature can be divided by their dimensions: (I) 0-dimensional including silica nanoparticles<sup>20</sup> and carbon quantum dots<sup>21</sup>, (II) 1-dimensional including

<sup>1</sup>Department of Surface Coatings and Corrosion, Institute for Color Science and Technology, Tehran, Iran. <sup>2</sup>Qazvin Water and Wastewater Company, Qazvin, Iran. ✉email: mahdavian-m@icrc.ac.ir

nanofibers and nanotubes such as carbon fiber<sup>22</sup> and carbon nanotubes (CNT)<sup>23,24</sup>, (III) 2-dimensional including nanoplates and nanosheets such as graphene-based materials<sup>25–27</sup>, molybdenum disulfide<sup>28</sup>, layered double hydroxides (LDHs)<sup>29,30</sup>, and (IV) 3-dimensional including organic metal frameworks (MOF)<sup>31</sup> and zeolites<sup>32</sup>.

Glass fibers (GF) are probably the most widely used reinforcing fillers in polymer composites. These composites are excellent and have low density, robust thermal and chemical stability, high rigidity and strength, and superior corrosion resistance<sup>33</sup>. Although these properties, GF are also prone to a variety of defects such as cracking, delamination, and failure during loading. Many of the locations that cause these defects result from poor bonding between GF and matrix, which can affect the material's mechanical strength<sup>34,35</sup>. Thus, solving this limitation improves the imperfect surface adhesion between the fibers and the polymer matrix and prepares a multifunctional composite with robust mechanical and protective features. Researchers around the world reported that the most important practical solutions to overcome this limitation are: (1) using coupling agents in the polymeric matrix<sup>36,37</sup> and (2) surface treatment of fibers<sup>38</sup>. Various surface modification techniques have been utilized on GF to improve their interfacial interactions with polymeric matrices. Alkali treatment, acetylation, plasma treatment, and grafting are common surface modification approaches for GF<sup>39</sup>.

Zhao et al.<sup>37</sup> used polyhedral oligomeric silsesquioxanes as an efficacious coupling agent for surface modification of conventional carbon fibers. Results showed that the interfacial bonding solidity of the composites increased by enhancing the wettability and chemical linkage. In recent research, Wang et al.<sup>40</sup> used silane coupling agents to treat nano-SiO<sub>2</sub> in a cellulose matrix, and the results indicated the KH-550 as an optimum modifier. Also, Feng et al.<sup>41</sup> investigated the consequence of alkaline and organosilane modifications on the mechanical features of polypropylene composites improved with kenaf fibers and pineapple leaves. The results showed that mechanical properties increased with chemical treatments.

The aim of this study is the surface modification of GF with (3-aminopropyl) triethoxysilane (APTES) and utilize it in an epoxy matrix as a robust FRP. The mechanical properties, cathodic delamination resistance, and adhesion of the modified and unmodified FRP were investigated in this work. This study is novel from the previous publications as it studies for the first time the consequence of silanization of GF on the cathodic resistance of the final FRP coating system. The cathodic disbonding resistance measurements were accompanied by two complementary electrochemical techniques: electrochemical noise (EN) and electrochemical impedance spectroscopy (EIS).

## Experimental

**Materials.** APTES was acquired from Merck Millipore (Germany). GF (GF/chopped strand mat) were obtained from Tamasha company (Iran). Zinc phosphate (ZP10) was provided by Heubach (Germany). Mild steel (ST12, Foolad Mobarakeh, Iran) was used as the substrate, and industrial epoxy resin (Epiran 01 and Epiran 06) and hardener (polyamide/SH615 and polyamine/F205, respectively) were employed for the fabrication of primer and top coatings, respectively.

**Surface modification of GF.** A silane solution was made by stirring 20 g of APTES into a mixture of 70 g of ethanol and 30 g of deionized water. The pH was brought to 4 for the hydrolysis of APTES by adding acetic acid and stirring for 4 h at 25 °C. Afterward, the silane solution was sprayed onto the GF, and the modified fibers denoted as MGF, were maintained at 25 °C for 3 days and 2 h at 75 °C to speed up the completion of the condensation reactions. The illustrative procedure of the surface modification is depicted in Fig. 1.

**Characterization of GF and MGF.** Fourier transform infrared spectra (FTIR) of GF and MGF samples were obtained using utilizing a Perkin Elmer spectrometer over the wavenumber span of 400–4000 cm<sup>-1</sup>. Field emission-scanning electron microscopy (FE-SEM) was performed utilizing a TESCAN instrument to assess the surface morphology and structure of the specimens. The thermal behavior of GF was investigated by thermogravimetric analysis (TGA) employing a Mettler Toledo instrument. Measurements were conducted at the temperature span of 20–600 °C with 10 °C min<sup>-1</sup> heating rate.

**Water contact angle test.** A contact angle instrument (OCA 15 plus) was utilized to evaluate the wettability of the GF and MGF. In this experiment, a precisely measured droplet of deionized water (4 μL) was placed onto the compact GF and MGF under controlled conditions of 25 ± 2 °C and 30 ± 5% humidity. After a 10-s, the water droplet's appearance was captured using a Canon digital camera.

**Preparation of FRP samples.** The FRP samples were prepared for cathodic delamination and EIS measurements test. To this end, the carbon steel panels were polished with sandpaper, washed with xylene, and dried. Afterward, the plates were coated with an epoxy primer coating containing 10 wt% ZP10 anticorrosive pigment, 60 wt% epoxy resin (Epiran 01), 30 wt% hardener (polyamide). The coated panels were cured at 25 °C for 7 days and post-cured in an oven at 60 °C for 2 h. A sheet of GF was fixed on the coated plate, and the mixture of 66.6 wt% epoxy resin (Epiran 06) and 33.4 wt% hardener (polyamine) was applied onto the GF. Finally, the FRP specimens were cured at 25 °C for 7 days and post-cured in the oven at 60 °C for 2 h. A similar procedure was followed for MGF, and the final composite was denoted as MFRP.

**Mechanical and compatibility tests.** To evaluate the tensile strength and compatibility of GF and MGF in epoxy resin, the 6.5 mm × 12 mm × 100 mm specimen was prepared using silicone molds, following the same resin and curing conditions mentioned in "Water contact angle test". The tensile strength of specimens was

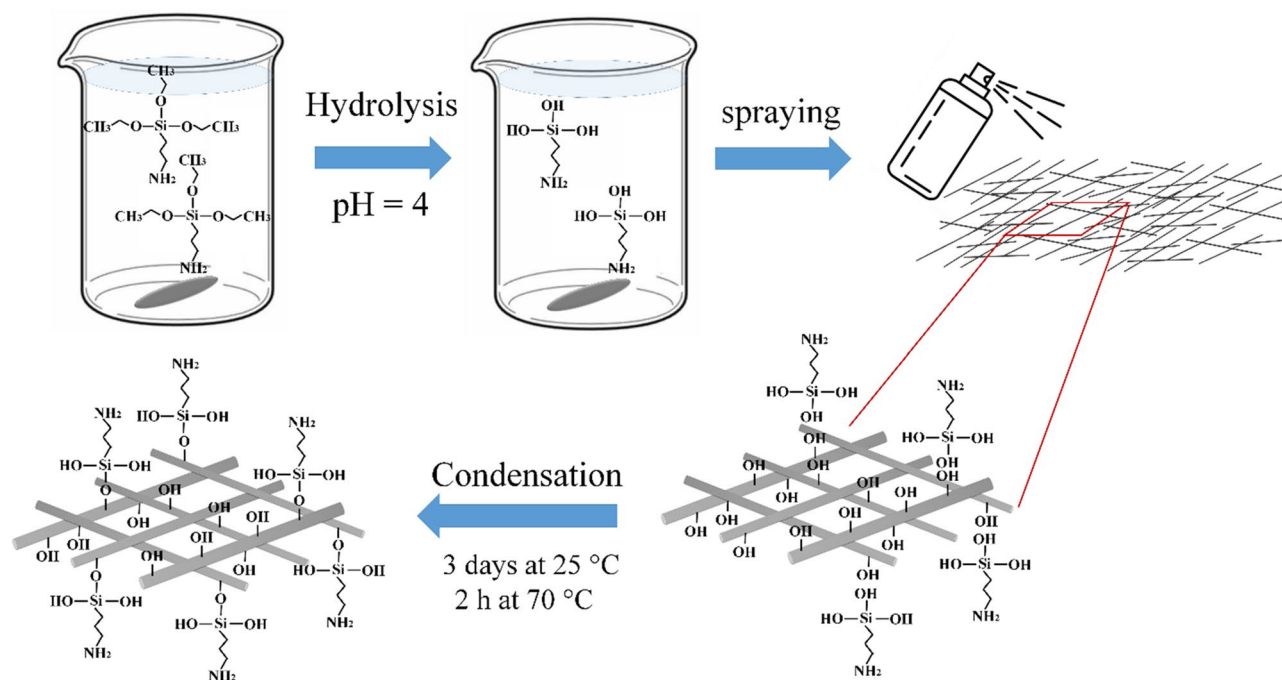


**Figure 1.** The schematic modification of GFs with APTES.

assessed by SANTAM (STM-5, EQSC1-22) instrument at the strain of  $5 \text{ mm min}^{-1}$ . The fracture area of the specimens was examined by SEM and EDS analysis utilizing the TESCAN instrument.

**Cathodic disbonding and electrochemical measurements.** The cathodic delamination measurements were taken from the specimens immersed in saline solution (3.5 wt% NaCl). A pit with 5 mm diameter was excavated at the center of the prepared FRP and MFRP samples ( $2 \text{ cm} \times 2 \text{ cm}$ ), and a potential of  $-1.5 \text{ V}$  vs. saturated calomel electrode (SCE) was imposed for 7 days in the 3.5% NaCl solution utilizing platinum wire as the counter electrode.

The EIS measurements were carried out from the sample before and after the cathodic delamination test using a three-electrode setup, including SCE as the reference electrode, FRP and MFRP coated specimens as working electrodes, and platinum as the counter electrode. The EIS measurement was implemented at open-circuit potential (OCP) in the frequency span of  $10 \text{ kHz} - 10 \text{ mHz}$ . The EIS data were fitted by ZSimpWin3.1 software.

The EN was implemented in a period of 800 s at 0.1 s intervals by connecting the two identical samples after 6 days of exposure to the cathodic delamination condition. The SCE was employed as the reference electrode. Wavelet transformation was utilized to remove the smooth crystal (DC trend) and to plot the relative amplitude of transients in the frequency domain.

**Adhesion strength measurement.** The pull-off test was conducted according to ASTM D4541 on all specimens in dry (before exposure to salt spray) and wet (after 720 h subjection to salt spray) states. The salt spray condition was in accordance with the ASTM B117. Adhesion measurements were conducted utilizing a PosiTest pull-off adhesion tester (DeFelsko, USA) at  $10 \text{ mm min}^{-1}$  velocity.

## Results and discussion

**Characterization of silanized GF.** Figure 2 illustrates the FTIR measurement results of modified and unmodified GFs. In the spectrum of neat GF, stretching vibrations of Si–O–Si can be observed at  $1043 \text{ cm}^{-1}$ , while bending vibrations take place at  $522$  and  $800 \text{ cm}^{-1}$ . The absorption bands at  $800$  and  $3433 \text{ cm}^{-1}$  could also be connected to Si–OH and hydroxyl group vibration, respectively. The absorption bands at  $2850$  and  $2924 \text{ cm}^{-1}$  are due to the stretching vibration of C–H in  $\text{CH}_2$  and  $\text{CH}_3$  groups. The bands at  $1630$  and  $1741 \text{ cm}^{-1}$  are analogous to the stretching vibration of C=C and C=O. Asymmetric and symmetric bending vibrations of C–H appeared at  $1382$  and  $1455 \text{ cm}^{-1}$ <sup>42–45</sup>.

Compared to the neat GF, some new peaks appeared, and some peaks have been intensified for MGF. The bands at  $702$ ,  $1040$ , and  $1116 \text{ cm}^{-1}$  are due to the Si–O–C vibrations, and the bands at around  $1430$  and  $3850$  are linked to the stretching vibration of C–H and N–H, respectively<sup>46,47</sup>. Moreover, the appearance of the peak at  $3743 \text{ cm}^{-1}$  was assigned to the unreacted silanol (Si–OH) group<sup>48</sup>. The magnitude of the band at  $1378 \text{ cm}^{-1}$  rises owing to the increment of Si–C and C–H groups<sup>49–51</sup>. Therefore, these results confirm the successful modification of GF with APTES.

Figure 3 illustrates the surface morphology and elemental composition of GF and MGF, which was evaluated by FE-SEM, EDS, and contact angle analysis. The FE-SEM image (shown in Fig. 3a) demonstrated that the GF is fibrous in shape, and the EDS confirmed that the strong peak belongs to silicon which showed that the main

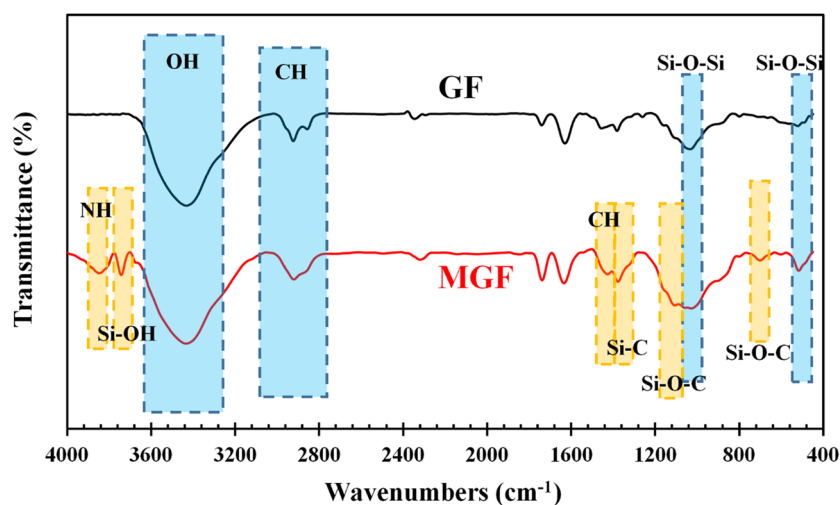


**Figure 2.** The ATR-FTIR spectra of GF and MGF.

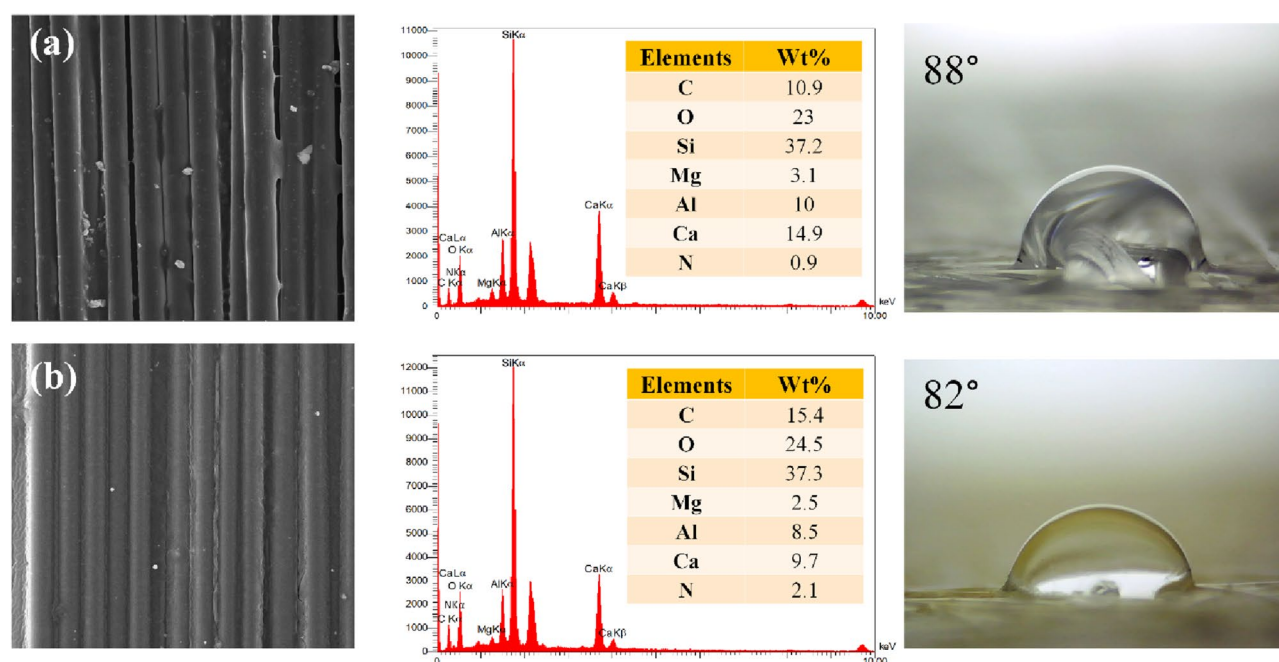


**Figure 3.** FESEM images, EDS analysis, and contact angle measurements of (a) GF and (b) MGF.

element of this sample is Si. Figure 3b revealed that the surface morphology of GF has not experienced any significant change after modification with APTES. The EDS analysis of GF illustrated that the weight ratio of O/Si is 0.62, which then rises to 0.66 for MGF. The composition (wt%) of carbon has increased from 10.9% in neat GF to 15.4% in MGF. The increase of the carbon, oxygen, and nitrogen content confirms the successful grafting of APTES on the surface of GF. The water contact angle results indicated a slight increase in the hydrophilicity of GF after modification which can be related to grafting APTES on the surface of GF and an increase in oxygen and nitrogen composition, confirmed by EDS results.

The thermogravimetric curves of GF and MGF are shown in Fig. 4. According to Fig. 4a, at the end of the test, the examined weight loss of MGF was about 4% higher than that of neat GF as the result of the APTES decomposition. The derivative thermogravimetric plots of two specimens are illustrated in Fig. 4b. The GF sample shows a single mass loss at around 350 °C attributed to the dehydroxylation. In addition to this weight loss, two other weight loss stages appeared for the MGF sample. The first one, centered at ca. 150 °C, is ascribed to the removal of water molecules due to the condensation of unreacted silanols groups. The second weight loss at 425 °C could be attributed to the decomposition of organic segments of APTES molecules<sup>52,53</sup>.

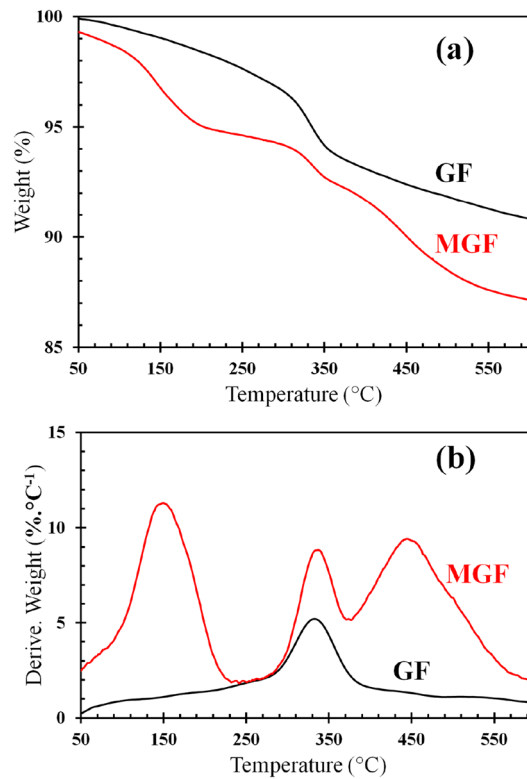


**Figure 4.** The TGA (a) and DTG (b) graphs of GF and MGF.

**Mechanical behavior of FRP.** The tensile stress–strain diagram of the composite reinforced with MGF and the GF is shown in Fig. 5. According to the curves, the elastic deformation is followed by plastic deformation. Upper yield point (assigned as 1 in Fig. 5), lower yield point (2), ultimate tensile strength (number 3), and elongation were obtained from the curves. Due to the more significant amount of pores and cracks in GF, lower elongation and tensile strength were obtained compared to the MGF specimen. The highest force reported for MGF was 625 N, and for GF was around 550 N. There were oscillations shown in the curves of GF in the plastic region. The test indicated that MGF exhibited higher mechanical behavior and tensile strength in comparison to the GF sample.

Fracture surfaces of the composites after the tensile test examined by FE-SEM are shown in Fig. 6. At the magnification of 1000 $\times$ ; it is evident that cracks and the formation of pores found on the surface of GF (illustrated

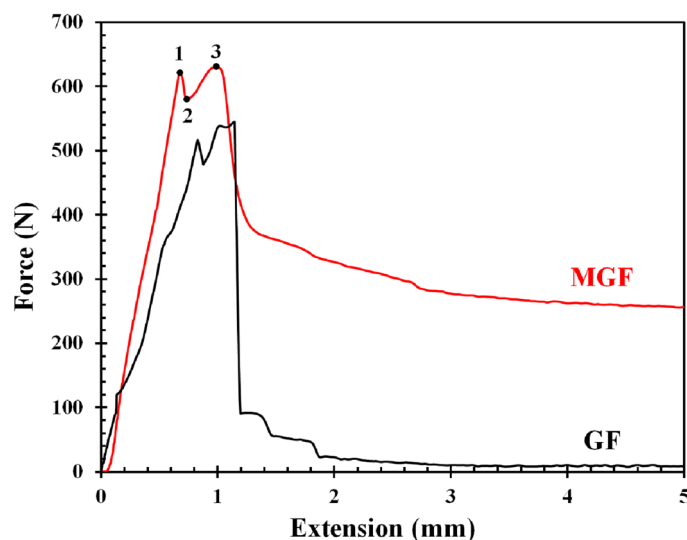


**Figure 5.** The tensile stress–strain test results of GF and MGF epoxy composites.

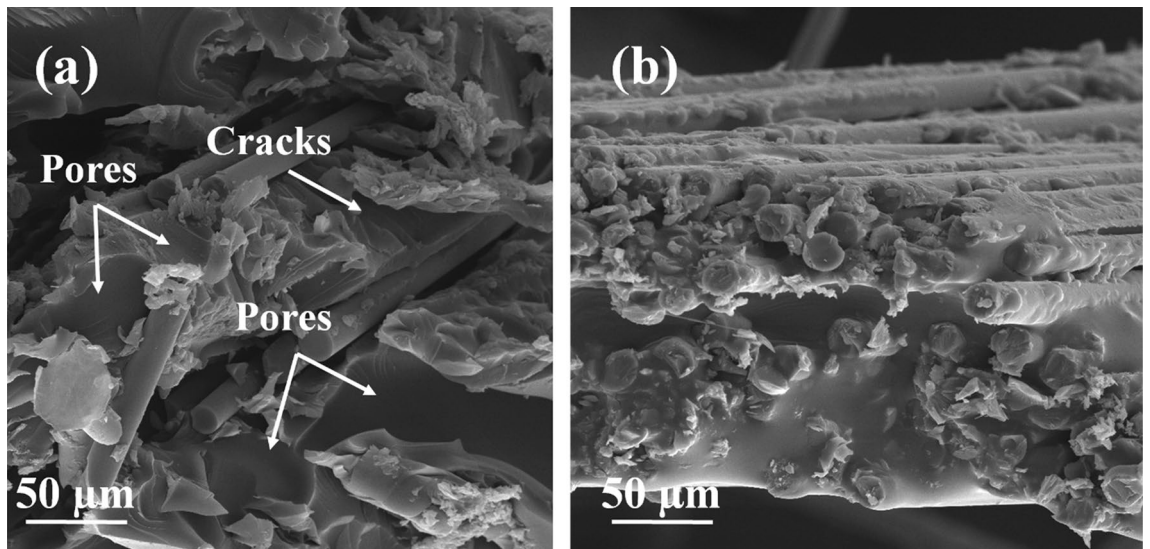


**Figure 6.** FESEM images of surface fracture of (a) GF and (b) MGF in epoxy composites.

in Fig. 6a), which can be the initial site of fracture and failure. On the surface of the fracture specimens of MGF, there are no traces of cracks and voids. This also proved the better mechanical behavior of the MGF sample. The amino groups of APTES, which are grafted to MGF, can chemically react to epoxide groups of epoxy resin and make excellent compatibility to the matrix and avoid cracks and voids initiation.

**Cathodic delamination resistance of FRPs.** The cathodic disbonding test was accomplished on the FRP and MFRP samples to investigate the adhesion of the coatings when the substrate was under cathodic protection. This method exerted the potential of  $-1.5$  V (vs SCE) to a mild steel substrate. The delaminated area of coatings was studied, and the outcomes are depicted in Fig. 7. The MFRP samples showed significantly lower delamination area compared to FRP, which can be referred to as less cathodic reactions at the metal/coating substrate due to fewer defects and pores in the MFRP coating. The water adsorbed in the coating during the time caused the cathodic reactions to take place beneath the coating and at the artificial hole. The cathodic reactions are shown in Eqs. (1) and (2). Due to releasing of hydroxyl ions, the pH at the interface was increased and caused the hydrolysis and destruction of coating/substrate bonding. The defects and pores in coatings cause the penetration of more water to the interface of coating/steel, enhancing the cathodic reaction, pH, and delamination:

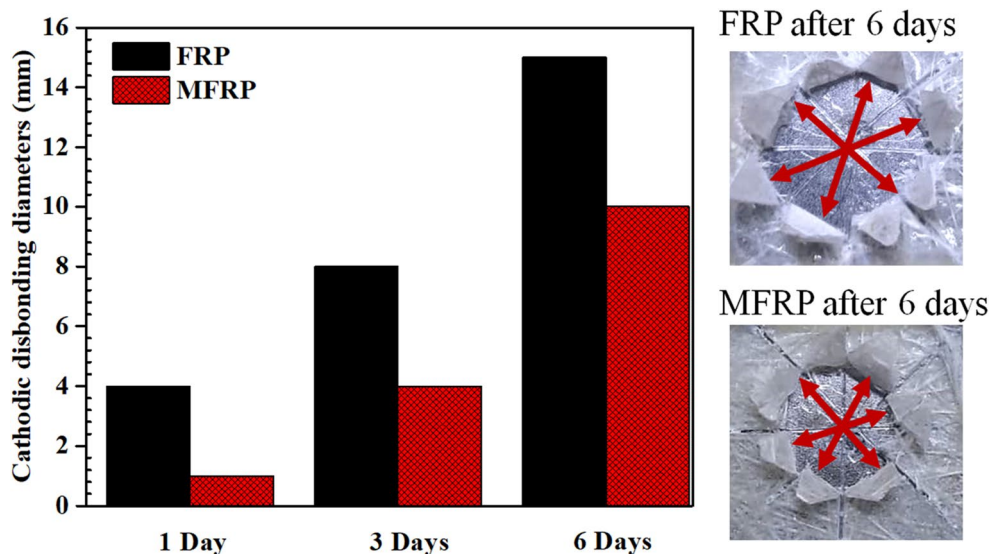
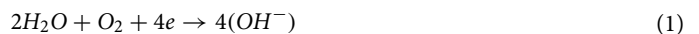


**Figure 7.** The visual delaminated area of FRP and MFRP during the cathodic delamination test.



Due to the high thickness of FRP coatings (approximately 0.5 mm), the delamination area of samples was further examined by EIS examination. The Nyquist and Bode diagrams of EIS results were depicted in Fig. 8a,b, respectively. From the Bode diagram, it can be seen that one relaxation time was attained, indicating the electrochemical reaction is under charge transfer control. The experimental results were simulated by a simple one-relaxation time-based electrical equivalent circuit (EEC) (Fig. 8), in which  $R_s$ ,  $R_{ct}$  and  $CPE_{dl}$  are, respectively, solution resistance, charge transfer resistance, and double layer constant phase element. The fitting results are provided in Table 1. The capacitance of the double layer is an appropriate parameter providing a measure of the delaminated surface, which was computed by Eq. (3)<sup>54</sup>:

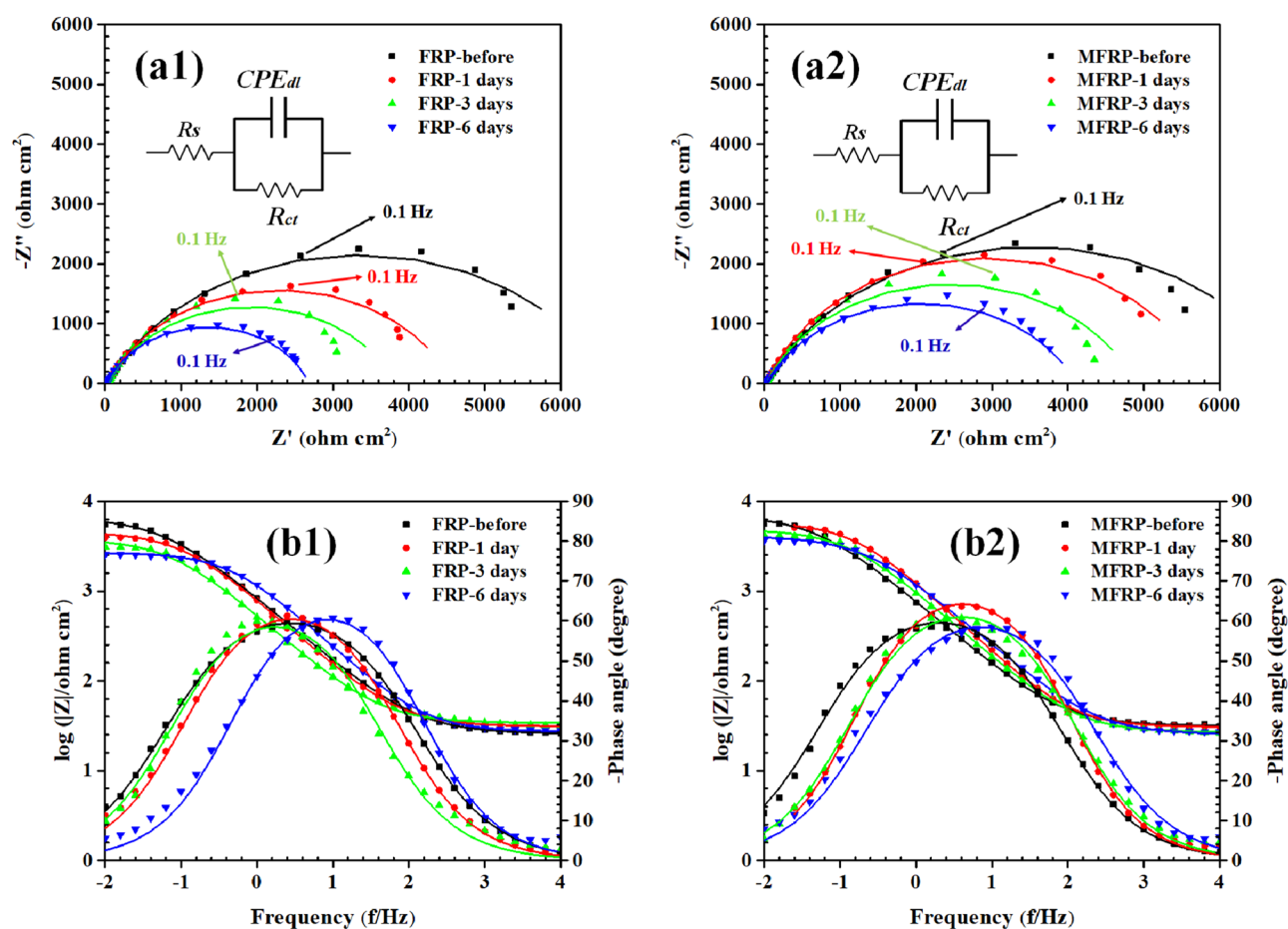


**Figure 8.** Nyquist plots of (a1) GF, (a2) MGF and Bod plots of (b1) GF, (b2) MGF from EIS measurements (symbols) and fitted data (line) during 6 days of exposure to the cathodic delamination condition.

Sample	Cathodic delamination time	$R_s$ (ohm $cm^2$ )	$R_{ct}$ (kohm $cm^2$ )	CPE <sub>dl</sub>	
				$Y_0$ (ohm <sup>-1</sup> $cm^{-2}$ s <sup>n</sup> )	$n$
FRP	Before test	27 ± 2	6.96 ± 0.7	3.25 × 10 <sup>-4</sup>	0.78 ± 0.03
	1 day	25 ± 1	6.6 ± 0.61	3 × 10 <sup>-4</sup>	0.8 ± 0.02
	3 days	31 ± 3	4.54 ± 0.34	2.9 × 10 <sup>-4</sup>	0.8 ± 0.06
	6 days	33 ± 2	3.78 ± 0.26	4.5 × 10 <sup>-4</sup>	0.75 ± 0.04
MFRP	Before test	29 ± 1	7.03 ± 0.45	3.32 × 10 <sup>-4</sup>	0.76 ± 0.05
	1 day	31 ± 4	6.98 ± 0.39	3.2 × 10 <sup>-4</sup>	0.75 ± 0.04
	3 days	30 ± 4	5.78 ± 0.31	1.7 × 10 <sup>-4</sup>	0.79 ± 0.06
	6 days	26 ± 2	4.85 ± 0.13	2.3 × 10 <sup>-4</sup>	0.76 ± 0.06

**Table 1.** Fitted EEC parameters of FRP and MFRP samples during the cathodic delamination test immersed in 3.5 wt% NaCl solution.

$$C_{dl} = Y_{0dl} \left( \frac{1}{n_{dl}} \right) \times \left( \frac{R_s + R_{ct}}{R_s \times R_{ct}} \right)^{\frac{(1-n_{dl})}{n_{dl}}} \quad (3)$$

where  $Y_{0dl}$  and  $n_{dl}$  are double-layer admittance and inhomogeneity-related constant of double layer, respectively. The total resistance ( $R_t = R_{ct} + R_s$ ) and  $C_{dl}$  of specimens before and during the cathodic delamination test were depicted in Fig. 9a,b, respectively. Before the test, the artificial hole of specimens was the same, which confirmed the similar  $R_t$  and  $C_{dl}$  of samples before the delamination test. The increment of  $C_{dl}$  and reduction of  $R_t$  result in spreading the delamination area over time. After 6 days of the cathodic delamination test, the  $C_{dl}$  and  $R_t$  ratios of MFRP/FRP coatings were 0.6 and 1.6, respectively, illustrating the high impact of MGF in epoxy coating's delamination resistance. The findings align with the information presented in the Bode diagrams (Fig. 9b). In the Bode plots, the time constant of the samples was associated with both the charge transfer resistance and the constant phase element (CPE). These elements exhibited a shift to higher frequencies as the immersion time increased, indicating an increase in the time constant ( $R_t \times C_{dl}$ ) values<sup>55,56</sup>.

Current noise transients derived from the wavelet transform are provided in Fig. 10. According to the figure, both FRP and MFRP shows the distribution of transients in the whole frequency range; however, MFRP shows a bit higher contribution of transients at higher frequency region, which might be ascribed to the less electrochemically active sites on the MFRP sample. The total energy of the current noise signal was 647 and 809  $\mu A^2$  for the MFRP and FRP, revealing a reduction in the active site on the mild steel due to the less delamination of the coating from the surface.

A schematic presentation of the effect of modification of GF on the cathodic delamination resistance is provided in Fig. 11. Presence of defects between unmodified GF and epoxy matrix provides a path for the water to penetrate in the FRP. In the case of MFRP, the MGF is wholly embedded in the epoxy matrix, and there is almost no defect at the MGF–epoxy interface. Water molecules take a longer path to reach the metal-coating interface.

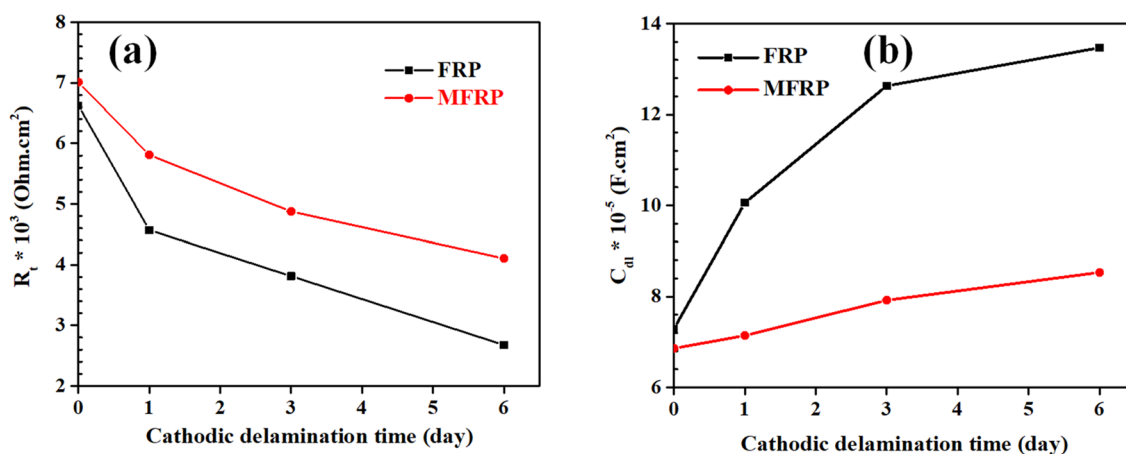


**Figure 9.** The FRP and MFRP's (a) total resistance ( $R_t$ ) and (b) double layer capacitance during 6 days of exposure to the cathodic delamination condition.

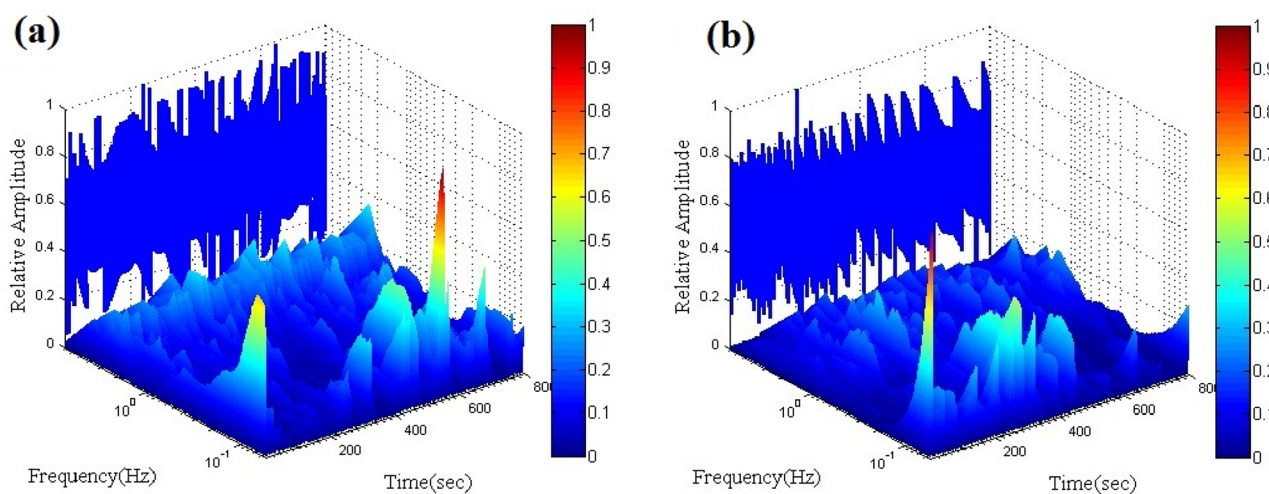


**Figure 10.** Electrochemical current noise signals from the FRP (a) and MFRP (b) samples after 6 days of exposure to the cathodic delamination condition.

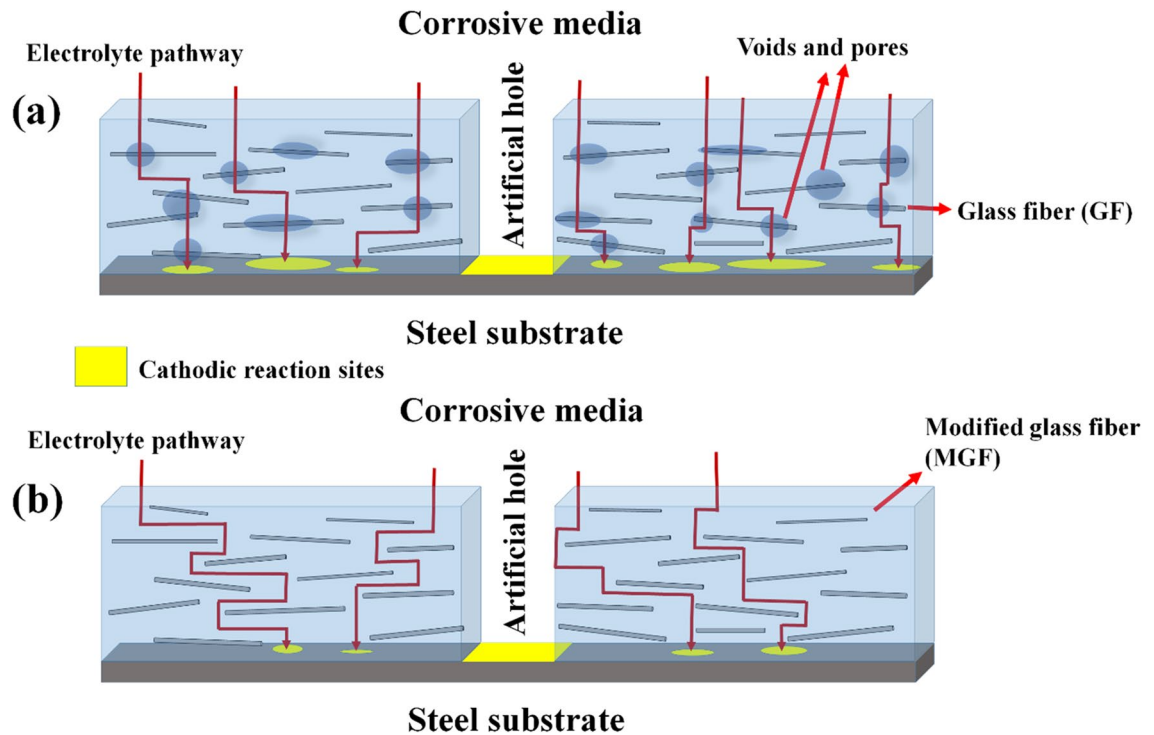


**Figure 11.** Schematic of water penetration and cathodic reaction sites in (a) FRP and (b) MFRP during cathodic delamination test.

The lower water penetration in MFRP compared to FRP reduces the cathodic reaction rates on the substrate surface, provoking less coating disbondment.

**Dry and wet adhesion strength measurements.** The pull-off measurement results are given in Fig. 12. In dry conditions, it is clear that the MFRP (3 MPa) had more adhesion strength compared to the unmodified specimen (2.1 MPa). The samples that underwent a 720-h salt spray test were considered in their wet state. The

	Dry condition	Wet condition
FRP		
	2.1 MPa	1.5 MPa
MFRP		
	3 MPa	2.7 MPa

**Figure 12.** Pull-off adhesion results under dry and wet condition for the FRP and MFRP samples.

adhesion results in the wet state revealed significantly higher adhesion strength for MFRP (2.7 MPa) compared to FRP (1.5 MPa). The adhesion loss percentage was calculated by Eq. (4):

$$\text{adhesion loss} = \left( \frac{D - W}{D} \right) \times 100 \quad (4)$$

where  $D$  and  $W$  are referred to the samples' strength of adhesion in dry and wet states. A lower adhesion loss was detected in the MFRP sample (10%) compared to the FRP (28%), reflecting improved durability of adhesion of the coatings upon surface modification of GFs.

## Conclusion

- The GFs were successfully modified by APTES through the condensation reaction of the hydroxyl groups of GFs and silanol groups of APTES.
- A cathodic delamination test evaluated the corrosion protection and compatibility of modified GFs. The visual cathodic delamination showed that the delamination area of the composite decreased by 34% after modification.
- The EIS results indicated a ca. 40% increase in double-layer capacitance and a ca. 40% decrease in the charge transfer resistance after 6 days of the cathodic delamination test, showing higher delamination of FRP compared to MFRP.
- The EN results also revealed a decrease in the current noise signal energy (ca. 20%) upon treatment of GFs, confirming the EIS results.
- The mechanical results of FRP and MFRP composites exhibited higher mechanical behavior and tensile strength upon treatment of GFs.
- According to the results of this work, the modification of GFs can effectively improve the FRP's cathodic resistance and mechanical strength.

## Data availability

All data generated or analyzed during this study are included in this published article.

Received: 26 February 2023; Accepted: 12 August 2023

Published online: 17 August 2023

## References

1. Matsuda, T., Kashi, K. B., Fushimi, K. & Gelling, V. J. Corrosion protection of epoxy coating with pH sensitive microcapsules encapsulating cerium nitrate. *Corros. Sci.* **148**, 188–197 (2019).
2. Jin, F.-L., Li, X. & Park, S.-J. Synthesis and application of epoxy resins: A review. *J. Ind. Eng. Chem.* **29**, 1–11 (2015).
3. Chen, P., Wang, Y., Li, J., Wang, H. & Zhang, L. Adhesion and erosion properties of epoxy resin composite coatings reinforced with fly ash cenospheres and short glass fibers. *Prog. Org. Coat.* **125**, 489–499 (2018).
4. Pour, Z. S., Ghaemy, M., Bordbar, S. & Karimi-Maleh, H. Effects of surface treatment of TiO<sub>2</sub> nanoparticles on the adhesion and anticorrosion properties of the epoxy coating on mild steel using electrochemical technique. *Prog. Org. Coat.* **119**, 99–108 (2018).
5. Jalili, M., Rostami, M. & Ramezanzadeh, B. An investigation of the electrochemical action of the epoxy zinc-rich coatings containing surface modified aluminum nanoparticle. *Appl. Surf. Sci.* **328**, 95–108 (2015).
6. Ramezanzadeh, B., Ghasemi, E., Askari, F. & Mahdavian, M. Synthesis and characterization of a new generation of inhibitive pigment based on zinc acetate/benzotriazole: Solution phase and coating phase studies. *Dyes Pigm.* **122**, 331–345 (2015).
7. Arman, S. Y., Ramezanzadeh, B., Farghadani, S., Mehdipour, M. & Rajabi, A. Application of the electrochemical noise to investigate the corrosion resistance of an epoxy zinc-rich coating loaded with lamellar aluminum and micaeous iron oxide particles. *Corros. Sci.* **77**, 118–127 (2013).
8. Diraki, A. & Omanovic, S. Smart PANI/epoxy anti-corrosive coating for protection of carbon steel in sea water. *Prog. Org. Coat.* **168**, 106835 (2022).
9. Mostafatabar, A. H., Bahlakeh, G. & Ramezanzadeh, B. Designing a novel anti-corrosion metal-organic platform based on dual-action epoxy coating. *Prog. Org. Coat.* **170**, 107007 (2022).
10. Liu, X., Xiong, J., Lv, Y. & Zuo, Y. Study on corrosion electrochemical behavior of several different coating systems by EIS. *Prog. Org. Coat.* **64**(4), 497–503 (2009).
11. Alam, M. A., Sherif, E.-S.M. & Al-Zahrani, S. M. Fabrication of various epoxy coatings for offshore applications and evaluating their mechanical properties and corrosion behavior. *Int. J. Electrochem. Sci.* **8**, 3121–3131 (2013).
12. Liu, B., Fang, Z., Wang, H. & Wang, T. Effect of cross linking degree and adhesion force on the anti-corrosion performance of epoxy coatings under simulated deep sea environment. *Prog. Org. Coat.* **76**(12), 1814–1818 (2013).
13. Montazeri, S., Ranjbar, Z. & Rastegar, S. The correlation between adhesion durability and viscoelastic creep-recovery behavior in epoxy coatings. *Prog. Org. Coat.* **111**, 395–401 (2017).
14. Husain, A., Chakkamalayah, J. & Al-Bahar, S. Electrochemical impedance spectroscopy as a rapid technique for evaluating the failure of fusion bonded epoxy powder coating. *Eng. Fail. Anal.* **82**, 765–775 (2017).
15. Meng, F. *et al.* The influence of the chemically bonded interface between fillers and binder on the failure behaviour of an epoxy coating under marine alternating hydrostatic pressure. *Corros. Sci.* **101**, 139–154 (2015).
16. Buchheit, R. G., Guan, H., Mahajanam, S. & Wong, F. Active corrosion protection and corrosion sensing in chromate-free organic coatings. *Prog. Org. Coat.* **47**(3–4), 174–182 (2003).
17. Motamedi, M., Ramezanzadeh, M., Ramezanzadeh, B. & Mahdavian, M. One-pot synthesis and construction of a high performance metal-organic structured nano pigment based on nanoceria decorated cerium (III)-imidazole network (NC/CIN) for effective epoxy composite coating anti-corrosion and thermo-mechanical properties impro. *Chem. Eng. J.* **382**, 122820 (2020).
18. Ramezanzadeh, B., Ghasemi, E., Mahdavian, M., Changizi, E. & Mohamadzadeh Moghadam, M. H. Covalently-grafted graphene oxide nanosheets to improve barrier and corrosion protection properties of polyurethane coatings. *Carbon* **93**, 555–573 (2015).

19. Haddadi, S. A., Ramazani, S. A. A., Mahdavian, M., Taheri, P. & Mol, J. M. C. Mechanical and corrosion protection properties of a smart composite epoxy coating with dual-encapsulated epoxy/polyamine in carbon nanospheres. *Ind. Eng. Chem. Res.* **58**(8), 3033–3046 (2019).
20. Fu, J. *et al.* Acid and alkaline dual stimuli-responsive mechanized hollow mesoporous silica nanoparticles as smart nanocontainers for intelligent anticorrosion coatings. *ACS Nano* **7**(12), 11397–11408 (2013).
21. Zhu, C. *et al.* Negatively charged carbon nanodots with bacteria resistance ability for high-performance antibiofilm formation and anticorrosion coating design. *Small* **15**(23), 1900007 (2019).
22. Liu, A. *et al.* In-situ growth of layered double hydroxides nanosheet arrays on graphite fiber as highly dispersed nanofillers for polymer coating with excellent anticorrosion performances. *J. Taiwan Inst. Chem. Eng.* **104**, 330–340 (2019).
23. Gu, B.-E., Huang, C.-Y., Shen, T.-H. & Lee, Y.-L. Effects of multiwall carbon nanotube addition on the corrosion resistance and underwater acoustic absorption properties of polyurethane coatings. *Prog. Org. Coat.* **121**, 226–235 (2018).
24. Wei, H., Ding, D., Wei, S. & Guo, Z. Anticorrosive conductive polyurethane multiwalled carbon nanotube nanocomposites. *J. Mater. Chem. A* **1**(36), 10805 (2013).
25. Ding, R. *et al.* A brief review of corrosion protective films and coatings based on graphene and graphene oxide. *J. Alloy. Compd.* **764**, 1039–1055 (2018).
26. Cui, G. *et al.* A comprehensive review on graphene-based anti-corrosive coatings. *Chem. Eng. J.* **373**, 104–121 (2019).
27. Zhao, Z., Zhou, M., Zhao, W., Hu, J. & Fu, H. Anti-corrosion epoxy/modified graphene oxide/glass fiber composite coating with dual physical barrier network. *Prog. Org. Coat.* **167**, 106823 (2022).
28. Ding, J., Zhao, H., Zhao, X., Xu, B. & Yu, H. How semiconductor transition metal dichalcogenides replaced graphene for enhancing anticorrosion. *J. Mater. Chem. A* **7**(22), 13511–13521 (2019).
29. Guo, L. *et al.* Layered double hydroxide coatings on magnesium alloys: A review. *J. Mater. Sci. Technol.* **34**(9), 1455–1466 (2018).
30. Zhang, F. *et al.* Self-healing mechanisms in smart protective coatings: A review. *Corros. Sci.* **144**, 74–88 (2018).
31. Zhang, M., Ma, L., Wang, L., Sun, Y. & Liu, Y. Insights into the use of metal-organic framework as high-performance anticorrosion coatings. *ACS Appl. Mater. Interfaces* **10**(3), 2259–2263 (2018).
32. Rassouli, L., Naderi, R. & Mahdavian, M. Study of the active corrosion protection properties of epoxy ester coating with zeolite nanoparticles doped with organic and inorganic inhibitors. *J. Taiwan Inst. Chem. Eng.* **85**, 207–220 (2018).
33. Saleem, A., Mushtaq, A., Khan, R. M., Ahmed, R. & Ali, Z. U. Enhance the corrosion resistance of underground petroleum tanks with the use of fiberglass reinforced composite. *Iran. J. Chem. Chem. Eng.* **20**, 20 (2023).
34. Ren, D. *et al.* Modification on glass fiber surface and their improved properties of fiber-reinforced composites via enhanced interfacial properties. *Compos. B Eng.* **177**, 107419 (2019).
35. Zhang, H. *et al.* Understanding interfacial interactions of polydopamine and glass fiber and their enhancement mechanisms in epoxy-based laminates. *Compos. A Appl. Sci. Manuf.* **116**, 62–71 (2019).
36. Orue, A., Anakabe, J., Zaldua-Huici, A. M., Eceiza, A. & Arbelaz, A. The importance of fiber/matrix adhesion and annealing process in water uptake of PLA/PMMA matrix composites reinforced with sisal fibers: The effect of coupling agent addition. *J. Nat. Fibers* **20**, 1–12 (2022).
37. Zhao, F. & Huang, Y. Grafting of polyhedral oligomeric silsesquioxanes on a carbon fiber surface: Novel coupling agents for fiber/polymer matrix composites. *J. Mater. Chem.* **21**(11), 3695–3703 (2011).
38. Garg, M., Sharma, S. & Mehta, R. Role of curing conditions and silanization of glass fibers on carbon nanotubes (CNTs) reinforced glass fiber epoxy composites. *Compos. Interfaces* **24**(2), 233–253 (2017).
39. Jing, M., Che, J., Xu, S., Liu, Z. & Fu, Q. The effect of surface modification of glass fiber on the performance of poly(lactic acid) composites: Graphene oxide vs silane coupling agents. *Appl. Surf. Sci.* **435**, 1046–1056 (2018).
40. Wang, L., Tang, C., Wang, X. & Zheng, W. Molecular dynamics simulation on the thermodynamic properties of insulating paper cellulose modified by silane coupling agent grafted nano-SiO<sub>2</sub>. *AIP Adv.* **9**(12), 125134 (2019).
41. Feng, N. L., Malingam, S. D., Razali, N. & Subramonian, S. Alkali and silane treatments towards exemplary mechanical properties of kenaf and pineapple leaf fibre-reinforced composites. *J. Bionic Eng.* **17**(2), 380–392 (2020).
42. Chuang, C., Wu, C., Wu, K. & Sheen, H. Flame retardancy of water-based intumescent coatings with etherified melamine-formaldehyde and polyvinyl acetate copolymer hybrid resin. *J. Appl. Polym. Sci.* **137**(31), 49279 (2020).
43. Rodriguez, M. A., Liso, M. J., Rubio, F., Rubio, J. & Oteo, J. L. Study of the reaction of  $\gamma$ -methacryloxypropyltrimethoxysilane ( $\gamma$ -MPS) with slate surfaces. *J. Mater. Sci.* **34**(16), 3867–3873 (1999).
44. Fashaid, F. *et al.* Tactical tuning of mechanical and thermo-mechanical properties of glass fiber/epoxy multi-scale composites by incorporating N-(2-aminoethyl)-3-aminopropyl trimethoxysilane functionalized carbon nanotubes. *Iran. Polym. J.* **29**(10), 875–889 (2020).
45. Yu, Z., You, S. & Baier, H. Effect of organosilane coupling agents on microstructure and properties of nanosilica/epoxy composites. *Polym. Compos.* **33**(9), 1516–1524 (2012).
46. Ahmadi, A., Ramezanzadeh, B. & Mahdavian, M. Hybrid silane coating reinforced with silanized graphene oxide nanosheets with improved corrosion protective performance. *RSC Adv.* **6**(59), 54102–54112 (2016).
47. Xiao, W., Zhao, P., Deng, S. & Zhang, N. Anchoring H<sub>3</sub>PW<sub>12</sub>O<sub>40</sub> on 3-aminopropyltriethoxysilane modified graphene oxide: Enhanced adsorption capacity and photocatalytic activity toward methyl orange. *New J. Chem.* **39**(5), 3719–3727 (2015).
48. Cendejas, M. C. *et al.* Controlled grafting synthesis of silica-supported boron for oxidative dehydrogenation catalysis. *J. Phys. Chem. C* **125**(23), 12636–12649 (2021).
49. Cuoq, F. *et al.* Preparation of amino-functionalized silica in aqueous conditions. *Appl. Surf. Sci.* **266**, 155–160 (2013).
50. Tan, G., Zhang, L., Ning, C., Liu, X. & Liao, J. Preparation and characterization of APTES films on modification titanium by SAMs. *Thin Solid Films* **519**(15), 4997–5001 (2011).
51. Gude, K., Gunko, V. M. & Blitz, J. P. Adsorption and photocatalytic decomposition of methylene blue on surface modified silica and silica-titania. *Colloids Surf. A Physicochem. Eng. Aspects* **325**(1–2), 17–20 (2008).
52. Beltrán, F. R., de la Orden, M. U. & Martínez, U. J. Amino-modified halloysite nanotubes to reduce polymer degradation and improve the performance of mechanically recycled poly(lactic acid). *J. Polym. Environ.* **26**(10), 4046–4055 (2018).
53. Yang, S. *et al.* Effect of reaction temperature on grafting of  $\gamma$ -aminopropyl triethoxysilane (APTES) onto kaolinite. *Appl. Clay Sci.* **6263**, 8–14 (2012).
54. Yi, P., Dong, C., Xiao, K., Man, C. & Li, X. In-situ investigation of the semiconductive properties and protective role of Cu<sub>2</sub>O layer formed on copper in a borate buffer solution. *J. Electroanal. Chem.* **809**, 52–58 (2018).
55. Morozov, Y. *et al.* Epoxy coatings modified with a new cerium phosphate inhibitor for smart corrosion protection of steel. *Corros. Sci.* **159**, 108128 (2019).
56. Ma, I. W. *et al.* Development of active barrier effect of hybrid chitosan/silica composite epoxy-based coating on mild steel surface. *Surf. Interfaces* **25**, 101250 (2021).

## Acknowledgements

This study was funded by the Qazvin Water and Wastewater Company (Qazvin, Iran).

### Author contributions

M.M., F.A.S. conceived the idea and supervised the project. M.S., S.F., P.G., Z.A., S.G., F.S.H., ran the experiments and prepared the first draft and analysis of the results. M.M. edited the final version of the manuscript.

### Competing interests

The authors declare no competing interests.

### Additional information

**Correspondence** and requests for materials should be addressed to M.M.

**Reprints and permissions information** is available at [www.nature.com/reprints](http://www.nature.com/reprints).

**Publisher's note** Springer Nature remains neutral with regard to jurisdictional claims in published maps and institutional affiliations.



**Open Access** This article is licensed under a Creative Commons Attribution 4.0 International License, which permits use, sharing, adaptation, distribution and reproduction in any medium or format, as long as you give appropriate credit to the original author(s) and the source, provide a link to the Creative Commons licence, and indicate if changes were made. The images or other third party material in this article are included in the article's Creative Commons licence, unless indicated otherwise in a credit line to the material. If material is not included in the article's Creative Commons licence and your intended use is not permitted by statutory regulation or exceeds the permitted use, you will need to obtain permission directly from the copyright holder. To view a copy of this licence, visit <http://creativecommons.org/licenses/by/4.0/>.

© The Author(s) 2023